

Distinct Energy Budgets of Mars and Earth

Larry Guan¹ , Liming Li¹ , Ellen C. Creecy², Xun Jiang², Xinyue Wang² , Germán Martínez³ , Anthony D. Toigo⁴, Mark I. Richardson⁵, Agustín Sánchez-Lavega⁶ , and Yeon Joo Lee⁷

Peer Review The peer review history for this article is available as a PDF in the Supporting Information.

Key Points:

- We generate the first meridional profiles of Mars' radiant energy budget at seasonal and annual scales, then compare them to those of Earth
- Mars' annual radiant energy budget shows deficits in the tropics and surpluses at other latitudes, while Earth's configuration is opposite
- Global dust storms significantly modify the radiant energy budget of Mars

Supporting Information:

Supporting Information may be found in the online version of this article.

Correspondence to:

L. Guan,
ljguan@uh.edu

Citation:

Guan, L., Li, L., Creecy, E. C., Jiang, X., Wang, X., Martínez, G., et al. (2024). Distinct energy budgets of Mars and Earth. *AGU Advances*, 5, e2024AV001389. <https://doi.org/10.1029/2024AV001389>

Received 10 JUL 2024
Accepted 27 OCT 2024

Author Contributions:

Conceptualization: Larry Guan,

Liming Li, Ellen C. Creecy, Xun Jiang

Data curation: Larry Guan, Liming Li, Ellen C. Creecy

Formal analysis: Larry Guan, Liming Li, Ellen C. Creecy, Xun Jiang, Xinyue Wang, Germán Martínez, Anthony D. Toigo, Mark I. Richardson, Agustín Sánchez-Lavega, Yeon Joo Lee

Funding acquisition: Liming Li, Xun Jiang

Investigation: Larry Guan, Liming Li

Methodology: Larry Guan, Liming Li

Project administration: Larry Guan, Liming Li

© 2024. The Author(s).

This is an open access article under the terms of the [Creative Commons Attribution License](https://creativecommons.org/licenses/by/4.0/), which permits use, distribution and reproduction in any medium, provided the original work is properly cited.

¹Department of Physics, University of Houston, Houston, TX, USA, ²Department of Earth and Atmospheric Sciences, University of Houston, Houston, TX, USA, ³Lunar and Planetary Institute, Houston, TX, USA, ⁴Applied Physics Laboratory, Johns Hopkins University, Laurel, MD, USA, ⁵Aeolis Research, Chandler, AZ, USA, ⁶Departamento Física Aplicada, Universidad Del País Vasco, Bilbao, Spain, ⁷PRC for Climate and Earth Science, Institute for Basic Science, Daejeon, South Korea

Abstract The radiant energy budget (REB) is a fundamental physical parameter for planetary bodies, though studies constraining the REB for bodies beyond Earth are relatively limited. We generate the first meridional profiles of Mars' REB at seasonal and annual timescales through measurements based on long term multi-instrument observations from spacecraft orbiting Mars. Then, we compare our findings to Earth's REB using contemporary satellite data sets. Each planet exhibits remarkably distinct seasonal REB distributions due to differences in their orbital, atmospheric, and surface properties. Annually, Earth's REB exhibits a tropical energy surplus and a deficit at the poles. In contrast, Mars' annual REB displays an inverted meridional distribution with significant hemispheric asymmetry. Additionally, global dust storms significantly modify the Martian REB. Our observations are employable in future studies to improve models on Mars' general circulation, meteorology, and polar ice cap evolution.

Plain Language Summary The climate and weather patterns of a planet or moon are significantly influenced by its radiant energy budget (its solar energy absorbed vs. heat energy emitted). Here, we determine Mars' radiant energy budget averaged at each latitude per season. While Mars' global energy budget remains roughly balanced over the course of a Martian year, as expected for rocky planets, there is a significant imbalance within each season. Mars' southern hemisphere during its spring season is the most striking example. Not only is the strongest energy excess amongst all Martian seasons found here - this excess is also the largest in terms of areal coverage, spanning almost all southern latitudes. Such an energy surplus contributes to the development of Mars' atmospheric circulation and dust storms. The influence of global dust storms on the radiant energy budget is also examined. Finally, we compare Mars' radiant energy budget to that of Earth, which reveals dramatic differences in the meridional distribution of radiant energy at both seasonal and annual timescales between the planets. These differences are attributed to the unique properties of each planet and have profound impacts on their respective climate systems.

1. Introduction

When studying the thermal characteristics of a planetary body, the radiant energy budget (REB) is of fundamental importance. For the terrestrial planets, it is largely sufficient to consider only the absorbed solar flux and the emitted thermal power, with the REB being defined as the subtractive difference between these two quantities (Atreya et al., 1989). When the REB has a value of zero, we consider it to be balanced—unbalanced if nonzero. Should the body possess a substantial atmosphere, the top-of-atmosphere REB serves as the boundary conditions for its climate and atmospheric circulations. Particularly, an uneven spatial distribution of radiant energy across the body is one key factor that drives global circulation (Peixoto & Oort, 1992).

In many aspects, Mars and Earth are similar. For starters, their obliquities (25.2° vs. 23.4°) and rotation periods (24.66 vs. 24.00 hr) are comparable. Over annual timescales, the REBs of Mars and Earth are in approximate balance as expected of terrestrial planets (Read et al., 2016). Mars, however, displays a stronger seasonal cycle than that of Earth because of the orbital eccentricity. While Earth's orbit is nearly circular (eccentricity ~0.0167), Mars' orbit is more elliptical (eccentricity ~0.0935). Consequently, Mars' global-average insolation is approximately 1.5 times greater at perihelion than at aphelion. In contrast, the variation of global-average insolation is less than 10% over a terrestrial orbit. Additionally, seasons on Mars vary greatly in length, which differs from the roughly equal season lengths on Earth.

Resources: Larry Guan, Liming Li, Ellen C. Creecy
Software: Larry Guan, Liming Li, Ellen C. Creecy
Supervision: Liming Li
Validation: Liming Li, Ellen C. Creecy
Visualization: Larry Guan
Writing – original draft: Larry Guan, Liming Li
Writing – review & editing: Larry Guan, Liming Li, Ellen C. Creecy, Xun Jiang, Xinyue Wang, Germán Martínez, Anthony D. Toigo, Mark I. Richardson, Agustín Sánchez-Lavega, Yeon Joo Lee

As an aside, some studies regarding Earth have discerned a small, long-term imbalance toward net absorption, likely a consequence of increasing greenhouse gases and aerosols from anthropogenic activities (Hansen et al., 2005; L'Ecuyer et al., 2015; Read et al., 2016; Trenberth et al., 2016). As experienced here on Earth, even the smallest imbalances on a planet's global REB can have massive implications on a planet's climate system. Currently, there is no consensus on whether a small imbalance exists for Mars because existing Martian observations lack the necessary spatiotemporal coverage to confidently discern such an imbalance.

Both Mars and Earth are among the handful of Solar System bodies possessing an atmosphere and ice caps at their poles. The key differences are: (a) the Martian atmosphere is much thinner than Earth's and overwhelmingly comprises carbon dioxide (CO₂), and (b) the Martian ice caps are mostly solid CO₂ instead of water ice, though residual water ice does exist on Mars underneath the frozen CO₂ at the north pole (Byrne et al., 2008). Unlike the Earth, Mars' atmosphere is subject to large seasonal pressure variations due to the exchange of CO₂ between its polar ice caps and atmosphere over the course of a year (Hourdin et al., 1993). Amounting to approximately a quarter of the total atmospheric CO₂ content, this phenomenon is primarily induced by seasonal variations of insolation and the subsequent distribution of the REB at the poles (Haberle & Kahre, 2010; Kelly et al., 2006; Martínez et al., 2017). The observational characteristics of Mars' REB provided in this study have potential for estimating or constraining the condensation and sublimation budgets of CO₂ in the polar regions, which plays a critical role in the CO₂ cycle and polar cap stability (Byrne, 2009; Byrne et al., 2008; Kieffer et al., 2000; Kieffer & Titus, 2001; Piqueux et al., 2015).

The meridional distribution of REB also has crucial influence on planetary surface, atmosphere, and climate (Atreya et al., 1989; Peixoto & Oort, 1992; Read et al., 2016; Schubert & Mitchell, 2014), so we analyze the meridional (zonally averaged) profiles of Mars' REB at seasonal and annual timescales. The meridional profiles of Mars' REB are analyzed using long-term observations from the Thermal Emission Spectrometer on the spacecraft Mars Global Surveyor (MGS-TES) (Christensen et al., 1998, 2001). On Mars, the most common source of meteorological variability is the dust storm, unlike Earth's liquid H₂O precipitation. Hundreds of dust storms occur every Martian year (MY) (Cantor et al., 2001)—some even reach global dominance (e.g., Battalio & Wang, 2021; Guzewich et al., 2019; Sánchez-Lavega et al., 2019; Smith et al., 2001; Strausberg et al., 2005; Zurek & Martin, 1993). MGS-TES observed one global dust storm in MY25, so we can explore the role of the global dust storm in the REB of Mars. Finally, we conduct a comparative analysis of the Martian REB to Earth's with respect to meridional distribution. Corresponding meridional profiles for Earth's REB are constructed with data from Clouds and the Earth's Radiant Energy System Energy Balanced and Filled (CERES-EBAF) (Loeb et al., 2018).

2. Materials and Methods

Analyses of the meridional profiles of REB at the seasonal and annual scales for Mars and Earth are based on the observations recorded by MGS-TES (Christensen et al., 1998, 2001) and CERES-EBAF (Loeb et al., 2018), respectively. The process of computing the radiant energy components (the absorbed solar energy and the emitted thermal energy) with the observations from MGS-TES and CERES-EBAF are described here, with corresponding plots for each step provided in Figures S1–S13 in Supporting Information S1.

2.1. Processing TES Data Sets

MGS-TES consists of a solar reflector sensor (0.3–2.9 μm) and a broadband thermal radiance sensor (5.1–150 μm) (Christensen et al., 1998). The observations recorded by the solar sensor are used to measure the reflected solar radiance and hence the absorbed solar power, while the observations recorded by the thermal sensor are used to measure the emitted thermal power. Here, we briefly detail the procedure of computing Mars' absorbed and emitted powers at both seasonal and annual timescales with the TES measurements.

With the known values of incident solar flux at Mars (Figure S1 in Supporting Information S1), the absorbed solar power can be computed by subtracting the reflected solar radiance from the incident solar flux. Meridional profiles of the incident solar flux at Mars are based on Mars' solar flux in the two-dimensional domain of Ls and latitude presented in our previous study of Mars' emitted power (Creecy et al., 2022). Figure S1 in Supporting Information S1 provides the meridional profiles at both seasonal and annual scales. For the observations of the reflected solar radiance, the TES team further processed them into albedo data by assuming a Lambertian surface for Mars (Christensen et al., 2001). We inherit this assumption because there is good agreement between the

collocated TES-derived Lambert-albedo values and the in-situ measurements from rovers (e.g., Perseverance) (Martínez et al., 2023).

Uncertainties that appear when using the Lambert albedo to represent the true albedo arise from two dominant sources: (a) the calibration of the reflected solar radiance data from TES; and (b) the non-Lambertian effect of Mars' surface. For the TES reflected solar radiance, the TES introductory paper suggests that the calibration error is roughly equivalent to a signal-to-noise ratio $\sim 2,300$, or $\sim 1/2,300$ ($\sim 0.04\%$) of the recorded solar radiance (Christensen et al., 2001). Such an error is about two orders of magnitude smaller than the error introduced by the non-Lambertian effect as discussed below. One previous study suggests that the non-Lambertian effect for the Martian surface is $\sim 9\%$, where terrain variations are responsible for ~ 4 of those 9% points (Bell et al., 2008). The 4% spatial variations for surface albedo have been accounted for in our computations of the zonal average albedo. Therefore, we systematically estimate the uncertainty in the albedo measurements as 5%, with its primary cause being the non-Lambertian effect. We further assume that 5% uncertainty for each pixel in the albedo maps (Figures S2 and S3 in Supporting Information S1) and for the meridional profiles of albedo in seasonal and annual timescales (Figure S4 in Supporting Information S1).

We first organize the TES data of Lambert albedo, which span from MY24 to MY28, into a 3-dimensional (3D) matrix (longitude \times latitude \times time). The areocentric solar longitude (L_s) is used to represent time in the TES data. Resolutions of the 3D matrix are 1° , 2° , and 10° for longitude, latitude, and L_s , respectively. The 3D matrix is averaged over L_s for each season to get the seasonal albedo maps (Figure S2 in Supporting Information S1). The four seasons in the northern hemisphere (NH) (spring, summer, autumn, and winter) have L_s ranges of $0\text{--}90^\circ$, $90\text{--}180^\circ$, $180\text{--}270^\circ$, and $270\text{--}360^\circ$, respectively. Based on the seasonal albedo maps, we can compute the annual-average global map of Mars' Lambert albedo after weighting each map by the varying lengths of each season (Figure S3 in Supporting Information S1).

It should be mentioned that Mars experienced a planet-encircling dust storm in the autumn of MY25. Global-scale dust storms can greatly influence the optical and thermal characteristics of Martian atmosphere (e.g., Battalio & Wang, 2021; Sánchez-Lavega et al., 2019), which has the potential to modify the absorbed solar power and emitted thermal power (Creedy et al., 2022). Since Earth experiences no global-scale phenomena of comparable size and severity, we exclude solar and thermal data from TES that is associated with the autumn of MY25 for the comparative study between Mars and Earth. This excluded data is repurposed for another part of this study, which investigates the role of the autumn MY25 global dust storm in Mars' REB.

Our previous study (Creedy et al., 2022) suggests that the global-average absorbed solar power, based on the TES global-average Lambert albedo, is smaller than the global-average emitted power during the TES epoch (MYs 24–28). There are two possibilities: (a) uncertainties in the measurements of Mars' albedo caused the inconsistency, and (b) there is indeed an energy imbalance at the annual scale. Sun-synchronous observations conducted by MGS-TES have incident angle limited coverage, making it difficult to fully examine the Bidirectional Reflectance Distribution Function and hence the regional albedo. Therefore, it is challenging to precisely measure the albedo and absorbed solar energy based on the TES observations, which further hinders our ability to examine the potential energy imbalance. It should be emphasized that the uncertainties in the albedo do not significantly affect the structure of meridional profiles of the albedo and its related absorbed solar power provided that the non-Lambertian effects and other unidentified error sources in albedo are systematic. Additionally, the uncertainty in the TES measurements of albedo (5%), as discussed above, is accounted for in our analysis of Mars' absorbed solar power and REB.

Earth's global-average annual REB is approximately balanced with an energy imbalance smaller than 0.1% of each of the radiant energy components (i.e., the absorbed solar energy and the emitted thermal energy) (Hansen et al., 2005; L'Ecuyer et al., 2015; Trenberth et al., 2016). In this study, we also assume that Mars' global-average REB at the annual scale is balanced despite lacking precise measurements. Our previous study of Mars' emitted power suggests that the global-average albedo at the annual scale should be 0.24 to balance the observed global-average annual emitted power (Creedy et al., 2022). Based on the annual-average Lambert albedo (Figure S3 in Supporting Information S1), the global-average albedo at the annual scale is 0.216. Consequently, each of the global maps of Mars' Lambert albedo in the four seasons are scaled by $0.24/0.216 = 1.12$, which corrects the Lambert albedo in adherence with the assumption of annual global power balance. The rescaled global maps are then averaged over the longitudinal direction to get the meridional profiles of Mars' albedo at both seasonal and annual scales (Figure S4 in Supporting Information S1).

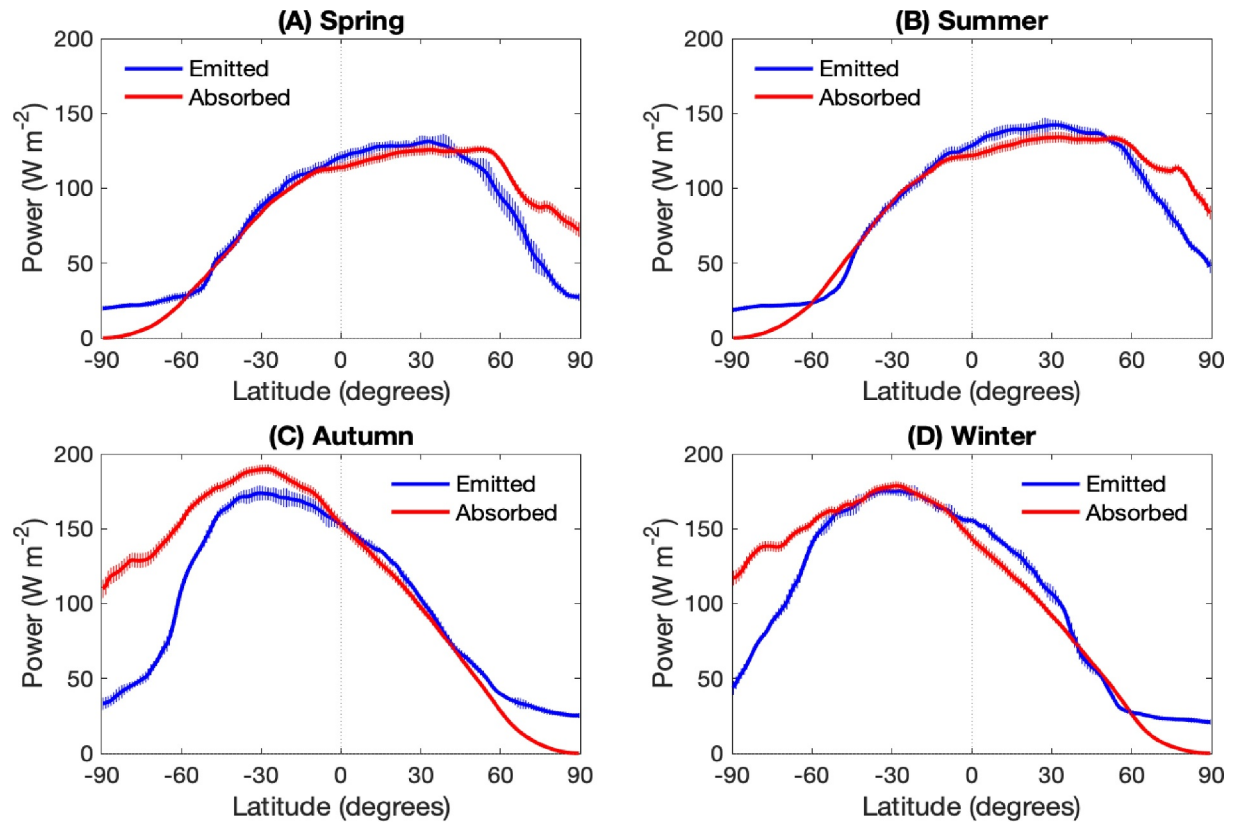


Figure 1. Seasonal comparison of meridional profiles between the absorbed and emitted powers of Mars. Vertical lines indicate uncertainties in the measurements of the absorbed and emitted powers. (a) Spring in the NH ($L_s = 0^\circ\text{--}90^\circ$), (b) Summer in the NH ($L_s = 90^\circ\text{--}180^\circ$), (c) Autumn in the NH ($L_s = 180^\circ\text{--}270^\circ$), and (d) Winter in the NH ($L_s = 270^\circ\text{--}360^\circ$). The average sub-solar latitudes for the four seasons are 16.2° , 16.7° , 15.6° , and 15.7° for the NH spring, summer, autumn, and winter, respectively.

The meridional profiles of Mars' albedo (Figure S4 in Supporting Information S1) are combined with the incident solar flux at Mars (Figure S1 in Supporting Information S1) to get the meridional profiles of absorbed solar power as follows: $P_{\text{abs}} = (1 - A)F$, where P_{abs} is the absorbed power, A the albedo, and F the incident solar flux. This equation suggests that uncertainty in the computed absorbed solar power is determined by uncertainties in both albedo and the incident solar flux. Incident solar flux is theoretically calculated based on known values of Mars' obliquity and the Sun-Mars distance, so its uncertainty is negligible. Therefore, the uncertainty in the computed absorbed solar power is primarily driven by the uncertainty in albedo, which as described earlier, is systematically estimated as 5%. The meridional profiles of Mars' absorbed power at both seasonal and annual timescales, along with their uncertainties, are presented in Figure S5 in Supporting Information S1.

Measurements of Mars' emitted power are based on observations recorded by the TES thermal sensor, with its processing previously completed using techniques originally developed to investigate the emitted power of Saturn, and later Titan and Jupiter (Li et al., 2010, 2011, 2012). To summarize the procedure for calculating Mars' emitted power from our previous study (Creedy et al., 2022): TES infrared data sets from MYs 24–28 were averaged seasonally to produce meridional profiles of Mars' emitted power for each season, with a 2° latitude resolution (Creedy et al., 2022). These seasonal profiles were then used to derive the annual profiles of Mars' emitted power. Additionally, the meridional profile of Mars' emitted power for the autumn of MY25 (the season with a global dust storm) was also separately computed in that study. The uncertainties in the emitted power, primarily arising from two dominant error sources (the uncertainty related to the calibration of TES infrared data and uncertainty related to filling observational gaps) were discussed in detail in our previous study (Creedy et al., 2022). A reproduction of the results from this procedure is presented in Figure S6 in Supporting Information S1, where linear interpolation was used to double the resolution to 1° latitude. Comparisons of the meridional profiles of Mars' absorbed solar power and emitted power at the seasonal scale are shown in Figure 1 of this paper. As a supplement, the comparison between solar power and emitted power profiles at the annual scale

is provided in Figure S7 in Supporting Information S1. The difference between the meridional profiles of absorbed solar power (Figure S5 in Supporting Information S1) and emitted power (Figure S6 in Supporting Information S1) at both seasonal and annual scales defines the REB profiles, which are displayed in Figure S8 in Supporting Information S1.

2.2. Processing CERES-EBAF Data Sets

Unlike Mars, the meridional profiles of Earth's zonally averaged REB are comparatively well-studied—the earliest analyses date back to the infancy of satellite technology (Ellis & Vonder Haar, 1976; Vonder Haar et al., 1980). As of 2023, the most up-to-date measurements for Earth's top-of-atmosphere REB are from CERES-EBAF, which is a data product constructed through agglomerating the radiance measurements acquired by multiple CERES instruments onboard the Terra, Aqua, Suomi National Polar-Orbiting Partnership, and NOAA-20 satellites (Loeb et al., 2018). This data product is accessible online (Doelling, 2022), where the desired data is selectable for export via a configurable user interface. For this study, the all-sky monthly profiles for the top-of-atmosphere reflected shortwave solar flux, outgoing longwave thermal flux, and incident solar flux were extracted with the “climate year” option (i.e., monthly averages for 2005–2015) to smooth out transient effects on Earth's albedo and to act as a baseline for what constitutes average conditions in the Earth's atmosphere. To compute the seasonal and annual average profiles of the absorbed and emitted powers from the monthly mean data (Figures S9–S13 in Supporting Information S1), each month is assigned a weight based on the number of days it has within the season of interest. Additionally, February is treated as 28.25 days long; solstices and equinoxes are considered to occur on the 22nd of March, June, September, and December. As an example, the month of March has a weight of 31/365.25 in the annual average, 9/92 in spring, 22/90.25 during winter, and 0 otherwise.

For the CERES-EBAF data sets, measurement uncertainties were given as 2.5 W/m^2 for the meridional profiles of emitted longwave thermal flux, reflected shortwave solar flux, and incident shortwave solar flux (Loeb et al., 2018). The meridional profiles of incident solar flux at both seasonal and annual scales, along with the uncertainties (2.5 W/m^2), are presented in Figure S9 in Supporting Information S1. We subtract the reflected solar flux from the incident solar flux to obtain the absorbed solar power at the seasonal and annual scales (Figure S10 in Supporting Information S1). Since the incident solar flux and the reflected solar power both have a uniform uncertainty of $\pm 2.5 \text{ W/m}^2$ for all data points (Loeb et al., 2018), the uncertainty of the absorbed power is also uniform ($\sim 3.5 \text{ W/m}^2$) as derived from the propagation of additive errors ($(2.5^2 + 2.5^2)^{1/2} = 3.5 \text{ W/m}^2$). For the emitted thermal power, their meridional profiles at both seasonal and annual scales, along with the uncertainties (2.5 W/m^2), are presented in Figure S11 in Supporting Information S1.

Based on the meridional profiles of absorbed and emitted power at the seasonal scale, we have the comparisons between Earth's absorbed solar power and emitted power during the four seasons in the main text (Figure 2). A related comparison between Earth's absorbed and emitted power at the annual scale is presented in Figure S12 in Supporting Information S1. Additionally, the REB profiles at both seasonal and annual scales, which are based on the profiles of the absorbed solar power (Figure S9 in Supporting Information S1) and emitted power (Figure S10 in Supporting Information S1) are displayed in Figure S13 in Supporting Information S1.

3. Results

3.1. REB Comparisons Between Mars and Earth at Seasonal and Annual Scales

When discussing imbalances in the REB, we consider positive and negative signs to indicate a net energy excess and deficit respectively while zero suggests a perfect balance. We first consider the seasonal profiles of Martian radiant energy components (Figure 1). Direct comparison of Mars' seasonal absorbed solar power and emitted thermal power profiles suggest an energy deficit near the equator and the northern middle latitudes during the northern spring (Figure 1a). The energy deficit here is related to the smaller absorbed solar power, a consequence of a higher local albedo (Figures S2 and S4 in Supporting Information S1). The southern polar region also exhibits an energy deficit attributable to a stronger decrease in the absorbed solar power relative to that of the emitted thermal power toward the South Pole. On the contrary, the northern pole shows an energy excess during NH spring, which is primarily caused by a large solar flux and the resulting high absorbed solar power (Figure S5 in Supporting Information S1). Furthermore, lower albedo values near latitudes 60°N and 75°N also contribute to the energy excess in the northern polar region. Exhibited in Figure 1b (NH summer) are similar patterns for each

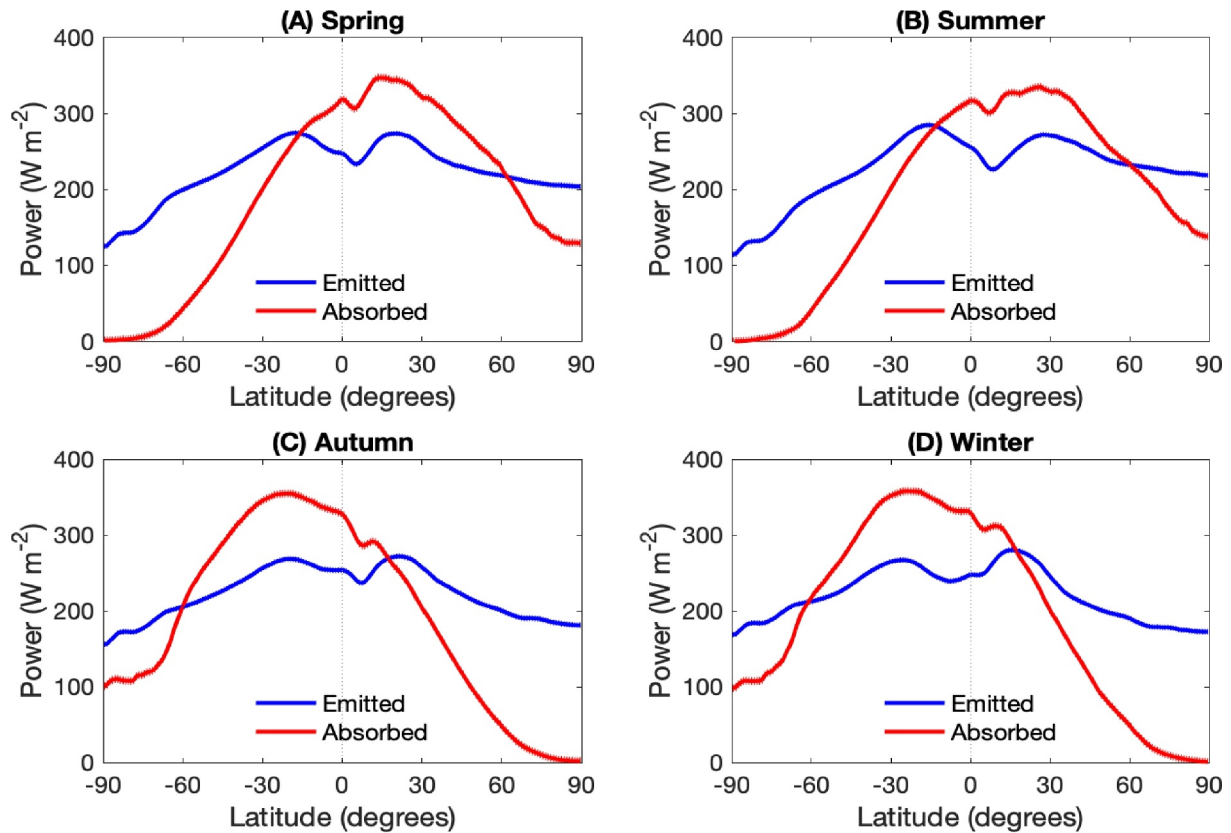


Figure 2. Seasonal comparison of the meridional profiles between Earth's absorbed and emitted powers. Vertical lines represent uncertainties in the absorbed and emitted powers. (a) Spring in the NH, (b) Summer in the NH, (c) Autumn in the NH, and (d) Winter in the NH.

radiant energy component as observed during the NH spring (Figure 1a), which rises from the comparable magnitudes of each component across the two seasons.

Panels C and D of Figure 1 also show similar patterns between the NH autumn and NH winter seasons, with a dominant energy excess in the southern hemisphere (SH) for both seasons. These two seasons occur around the perihelion of Mars' orbit (solar longitude $L_s = 251^\circ$), where the Sun-Mars distance is minimal and the solar flux is maximal. Thus, the strong solar flux in the SH during these seasons is the primary reason for the energy excesses observed there. Perihelion's occurrence within the northern autumn ($L_s = 180\text{--}270^\circ$) instead of the northern winter ($L_s = 270\text{--}360^\circ$) also explains the greater latitudinal range and magnitude of the former season's energy excess (panel C) compared to the latter (panel D).

Now, we examine the seasonal profiles of Earth's REB. Figure 2 shows minima near the equator for both absorbed solar power and emitted thermal power across all four seasons. Minima in the power absorption profiles are related to the high albedo deserts and clouds present at $\sim 10^\circ\text{N}$ latitude; minima in the emitted power profiles are attributed mostly to the high clouds generated by the Inter-Tropical Convergence Zone (Schneider et al., 2014). These high clouds, characterized by relatively cold temperatures, are the dominant depressor of equatorial power emission. Figure 2 further indicates that the regional minima around the equator are much more pronounced in the emission profiles compared to the absorption profiles, contributing to Earth's persistent tropical energy excesses across all seasons, which are more clearly illustrated in Figure 3. Figure 3 also shows that Earth's tropical energy excess shifts from a latitudinal band spanning $\sim 20^\circ\text{S}\text{--}60^\circ\text{N}$ during the NH spring and summer seasons to a latitudinal band of similar width shifted roughly 40° southward during the other two seasons. Outside the tropics, energy deficits are observed in the middle and high latitudes throughout all seasons.

Returning to Mars, the REB for each of the four seasons (red curves in Figure 3) is constructed based on the meridional profiles of each radiant energy component shown in Figure 1. Generally, energy imbalances are more pronounced in the polar regions ($>60^\circ$) than at lower latitudes. During the NH spring and summer, the northern

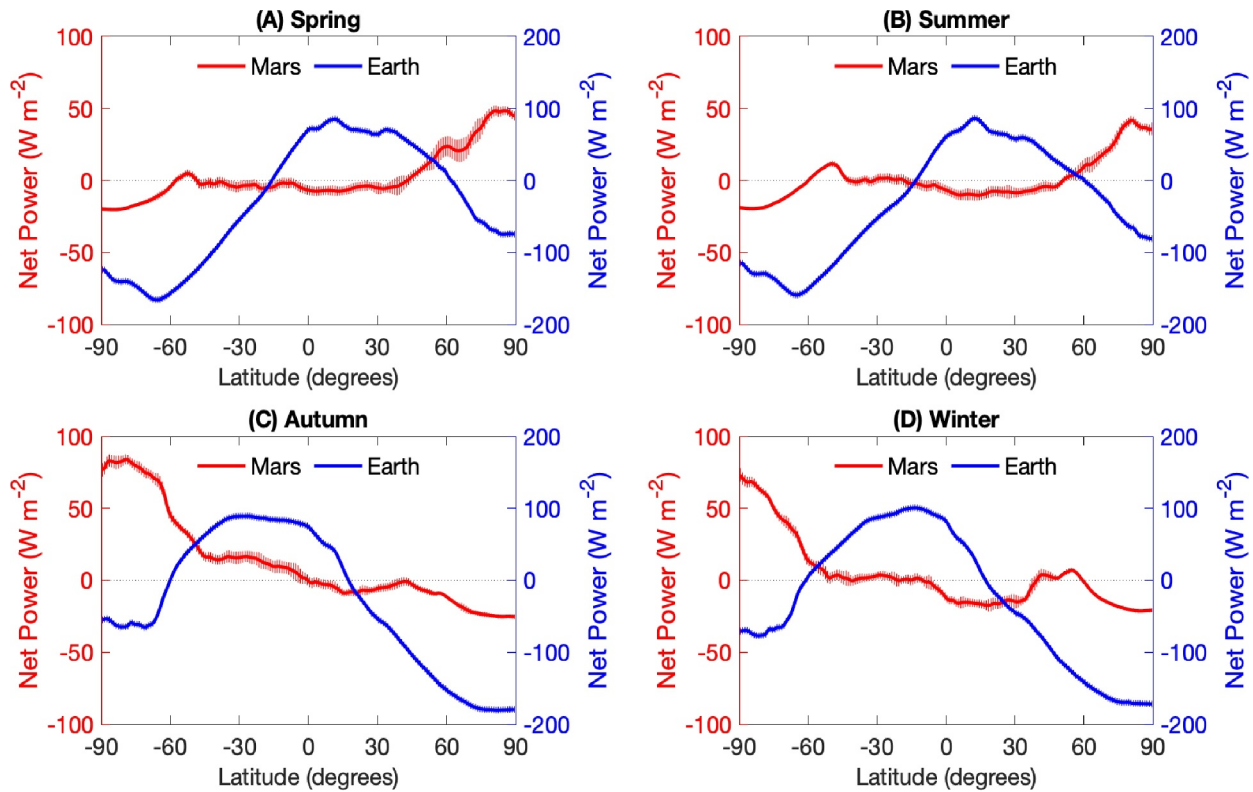


Figure 3. Seasonal comparison of meridional profiles of the REB (the absorbed power minus the emitted power) between Mars and Earth. Vertical lines indicate uncertainties of the REB. Different scales are used in the vertical axis for each planet to maintain the visibility of finer structure within the profiles. (a) Spring in the NH, (b) Summer in the NH, (c) Autumn in the NH, and (d) Winter in the NH.

polar region experiences an energy excess, while the southern polar region shows an energy deficit. In the other two seasons (NH autumn and winter), the polar regions reverse this pattern. An extreme case is observed in NH autumn (panel C of Figure 3), where an energy excess almost completely covers the SH, with the strongest magnitude of any season, reaching approximately 80 W/m^2 near the south pole.

Now, we consider the annual average energy imbalances of each planet (Figure 4). Derived from averaging the seasonal energy imbalance profiles of Figure 3, fundamental differences between these two terrestrial planets' REBs are reinforced. Once more, we observe an energy deficit predominant in the Martian tropics, while Earth's tropics exhibit an energy excess. Mars' tropical energy deficit is concentrated north of the equator, whereas Earth's tropical energy excess is roughly symmetric about the equator. The unique topography of each planet and their different orbital characteristics underly these differences at annual time scales.

Poleward, the annual average energy imbalance manifests different patterns as well, though the behavior follows that of the seasonal profiles. Martian middle and high latitudes have energy excesses, while deficits are found on Earth. Earth's deficits are largely due to its oceans and thick atmosphere acting as effective transporters of incident solar flux poleward from the tropics (Boeira Dias et al., 2020; Stocker et al., 2013). Conversely, Mars' thin atmosphere hinders efficient meridional solar flux transport, subsequently yielding a steeper meridional temperature gradient and thus a greater contrast in power emission between the tropics and higher latitudes of Mars (Figure 1) relative to Earth (Figure 2). This meridional contrast on Mars results in higher latitude energy excesses, while a smaller corresponding contrast on Earth contributes to energy deficits in its high latitudes (Figure 4).

3.2. Role of Global Dust Storms in Martian REB

During the period of TES observations, a global dust storm developed in the northern autumn of MY25. Therefore, TES observations of the MY25 global dust storm provide an opportunity to examine the role of how global dust storms modify Mars' REB. The impacts of the MY25 global dust storm on the emitted thermal power

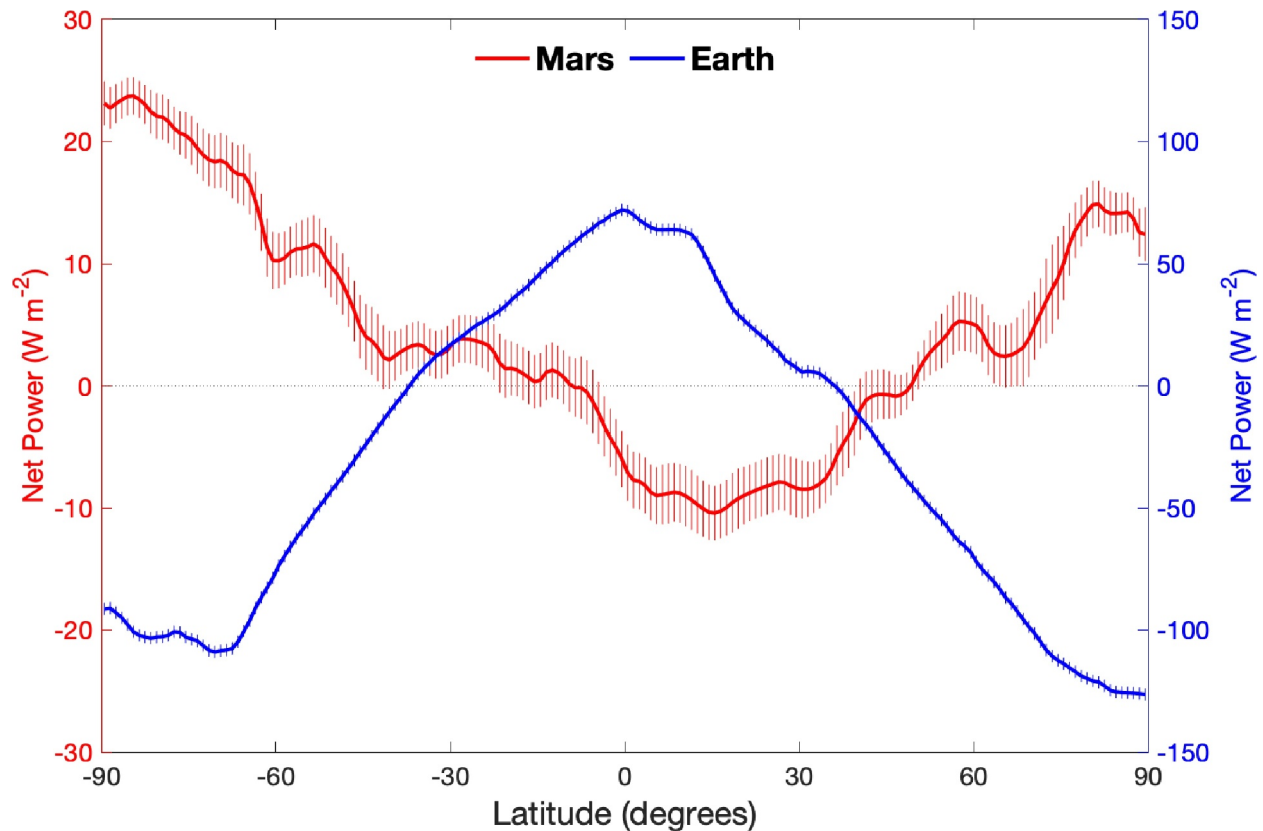


Figure 4. Comparison of annual-average meridional profiles of the REB between Mars and Earth. Vertical lines indicate uncertainties in the measurements of the REB.

were discussed in our previous study (Creedy et al., 2022). Here, we investigate the storm's influence on albedo and, by extension, the absorbed solar power. Then, in combining the analyses of emitted and absorbed powers, we can determine the role of the MY25 global dust storm in Mars' REB.

We begin by averaging the Lambert albedo from the TES data set during autumn MY25 to derive the seasonally averaged albedo. The global map of Lambert albedo in autumn of MY25 is then compared to the global map of other autumns without global dust storms (referred to as *normal autumns*—see Figures S14 and S15 in Supporting Information S1). There are noticeable changes in albedo from normal autumns to the autumn of MY25. In the Hellas basin ($\sim 40^\circ\text{S}$), where the global dust event originated, the albedo increased substantially. Elsewhere, the albedo increase can exceed 60%. Changes in albedo can be explained by increased dust transport during the global dust storm. These additional dust particles, both those suspended in the atmosphere and resting on the surface, reflect more sunlight and thereby increases the albedo.

Albedo increases are more pronounced southward of the Hellas basin than to the north. This is probably related to the asymmetry in the global meridional circulation, where the circulation branch in the northern hemisphere is stronger and wider than that of the southern hemisphere during the autumn season (e.g., Holmes et al., 2019, 2020). Generally, the magnitude of albedo modification decreases in latitude bands moving away from Hellas basin (Figure S15 in Supporting Information S1). In the southern polar region ($60\text{--}90^\circ\text{S}$), the albedo modification due to the global dust storm is more complex. Longitudes initially covered by polar ice ($\sim 120^\circ\text{W}\text{--}45^\circ\text{E}$) saw an increase in albedo, whereas other longitudes saw a decrease. This is because dust particles that cover polar ices decrease albedo, as Martian soil has lower reflectivity than ice, while in non-icy polar longitudes, dust particles aloft increase the albedo by reflecting more sunlight.

By averaging the albedo in the longitudinal direction, we obtain the meridional profiles of Lambert albedo for the autumn of MY25 and normal autumns. We then multiply these profiles by the scale factor of 1.12 as discussed earlier, which adjusts the Lambert albedo to a value that satisfies the assumption of a globally balanced annual

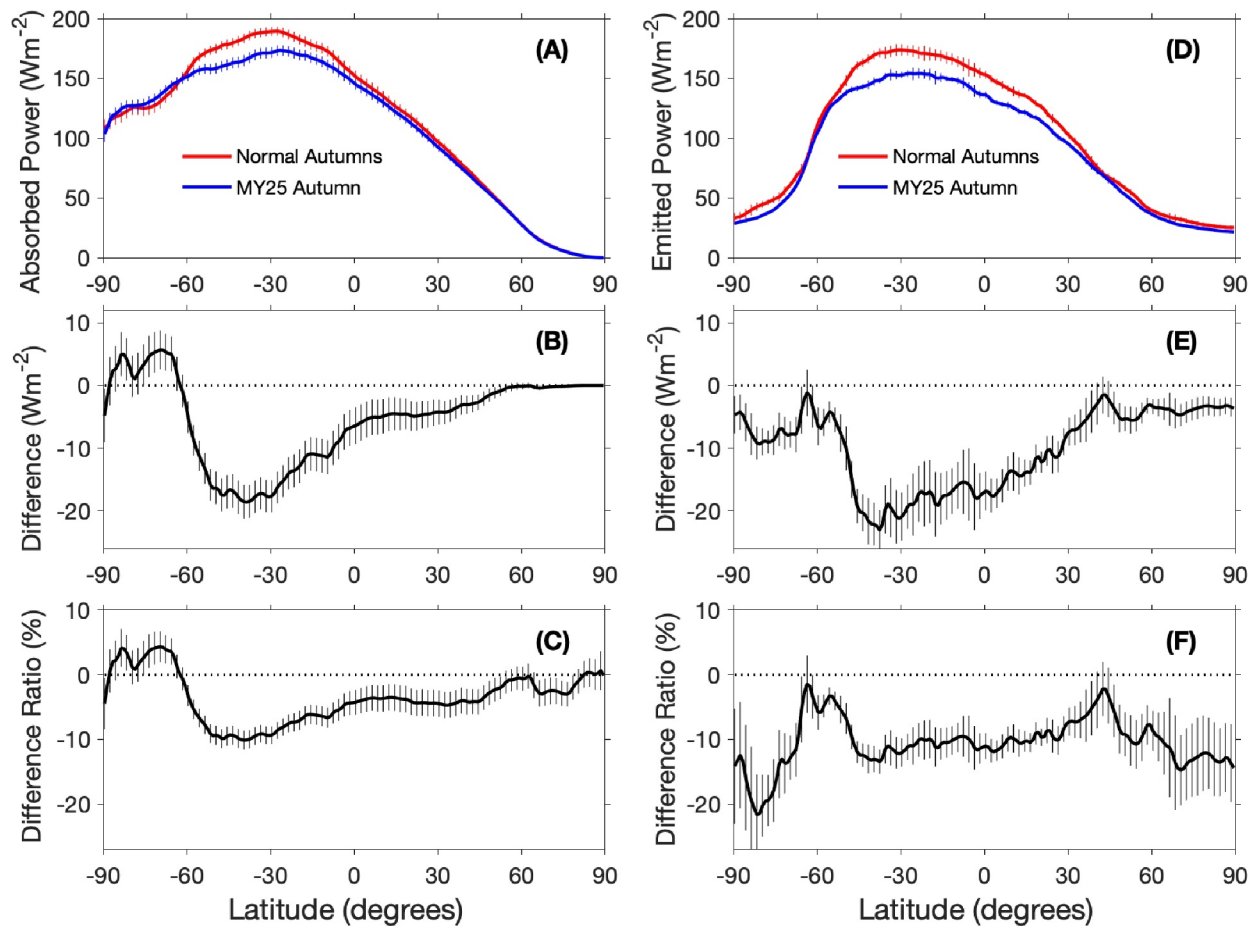


Figure 5. Comparison of the absorbed and emitted powers between normal autumns and the autumn of MY25. Vertical lines indicate measurement uncertainties. A global dust storm developed during the autumn of MY25, while autumns without global dust storms are defined as normal autumns. (a) Comparison of Mars' absorbed solar power between normal autumns and the MY25 autumn. (b) Difference—defined here as Mars' absorbed solar power in autumn MY25 minus that of normal autumns. (c) Difference ratio—the ratio between the difference (panel B) and the absorbed power of normal autumns (red line in panel A). Panels (d), (e), and (f) are the same as (a), (b), and (c), respectively except for the emitted thermal power.

energy budget. During the MY25 global dust storm, the maximum albedo increase occurs around $\sim 40^{\circ}\text{S}$, or where the Hellas basin lies. Simultaneously, the zonal mean albedo decreased in the southern polar region while increasing everywhere else from normal autumns to the autumn of MY25 (See Figure S16 in Supporting Information S1).

Based on the albedo modifications just described (Figure S16 in Supporting Information S1), we now examine the impact of the MY25 global dust storm on the absorbed solar power. Figure 5 shows the changes in the absorbed solar power versus variations in the emitted thermal power (Creedy et al., 2022). Increased albedo decreases absorbed solar power, so modifications of absorbed solar power caused by the global dust storm (panel B of Figure 5) are inversely related to changes in albedo (panel B of Figure S16 in Supporting Information S1). The maximum decrease in the absorbed solar power occurred in the latitude of Hellas basin ($\sim 40^{\circ}\text{S}$), with a reduction of $\sim 18 \text{ Wm}^{-2}$ ($\sim 10\%$). Panel E of Figure 5 shows that the emitted power also decreased during the season of the global dust storm (MY25 autumn), again particularly in the Hellas basin. However, unlike with absorbed solar power, the global dust storm decreased the emitted power across all latitudes (Creedy et al., 2022). During the day, dust particles in the atmosphere reflect and absorb solar radiation, which cools the surface (e.g., Gurwell et al., 2005; Smith, 2004) and subsequently reduces emitted power (Creedy et al., 2022). At night, dust particles in the atmosphere trap outgoing thermal radiation from the surface, causing surface temperatures and emitted power to rise. However, the overall effect of the global dust storm in MY25 was a decrease in the emitted power, as the daytime reduction outweighed the nighttime increase (Creedy et al., 2022).

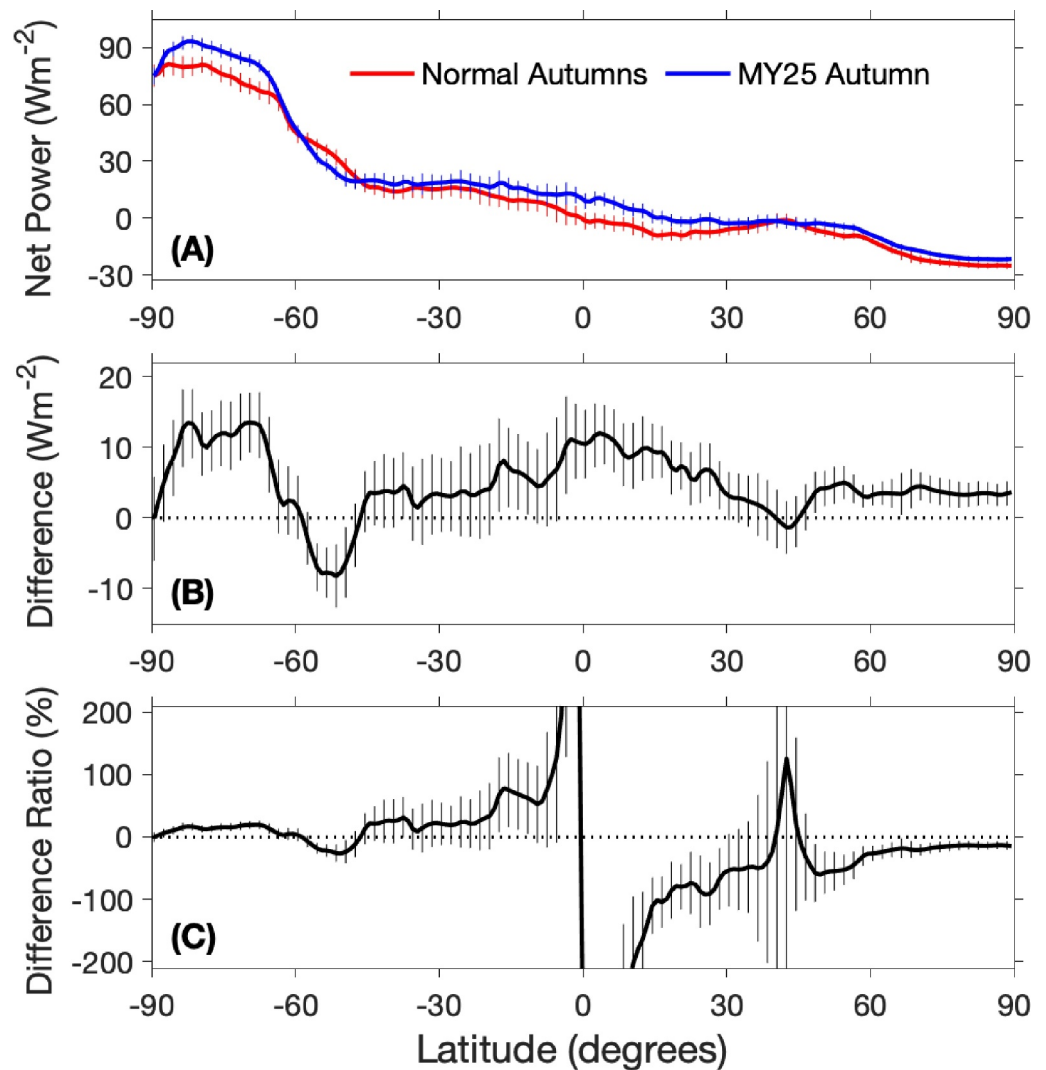


Figure 6. Comparison of the net power between normal autumns and the autumn of MY25. Vertical lines indicate measurement uncertainties. (a) Comparison of Mars' net power between normal autumns and autumn of MY25. (b) Difference between the net power of autumn MY25 minus and the net power in normal autumns. (c) Ratio between the difference (panel B) and the net power of normal autumns (red line in panel A). Extremely large difference ratios, resulting from the net power of normal autumns approaching zero near the equator, are not shown in panel C to maintain visibility of the finer structures within the middle and high latitudes.

By combining the variations in absorbed and emitted powers (Figure 5), we can next assess the impact of the MY25 global dust storm on the REB (i.e., the net power). Figure 6 suggests that the maximum increase in the net power caused by the storm mainly occurred in the southern polar region. At other latitudes, changes in the absorbed and emitted powers better offset each other, resulting in smaller net power variations. In most latitudes beyond the southern polar region, the decrease in the emitted power exceeds the decrease in the absorbed power, leading to an increase in the net power. Exceptions include a latitude band from $\sim 47^{\circ}S$ to $\sim 60^{\circ}S$ and a narrow band around $43^{\circ}N$, where the decrease in the emitted power was less than the decrease in the absorbed power, resulting in a decrease in the net power. Uncertainties in the net power variations are larger than the variations themselves at some latitudes, making these changes statistically insignificant. Additionally, the difference ratio (variation in the net power relative to the net power of normal autumns) becomes extremely large near the equator, where the net power approaches zero during normal autumns.

We conclude this section with a brief look into the hemispheric distribution of albedo between the planets. Unlike Mars, Earth does not experience singularly sourced global weather phenomena akin to Martian global dust

storms. Despite that, the annual-mean albedo and reflected solar power on Earth exhibit a surprisingly hemispheric symmetry (e.g., Datsieris & Stevens, 2021; Stephens et al., 2015). The CERES-EBAF data set shows that the hemispheric-average albedos are 0.29351 and 0.29396 for the NH and SH, respectively. The difference in albedo between the two hemispheres is $\sim 0.15\%$, which is much smaller than the measurement uncertainty ($\sim 1.0\%$). This hemispheric symmetry in Earth's albedo is attributed to a compensating mechanism, where increased reflection from clouds in the SH balances the higher reflection from land in the NH (e.g., Datsieris & Stevens, 2021; Stephens et al., 2015). However, current atmospheric and climate models fail to capture this symmetry (Stephens et al., 2015), suggesting an incomplete understanding of the underlying physics behind the hemispheric symmetry in Earth's albedo, even though there are some proposed mechanisms such as the role of clouds (Datsieris & Stevens, 2021). Since the observational characteristics of Earth's albedo have been used to evaluate the climate models of our home planet (e.g., Stephens et al., 2015), usage of Mars' albedo and REB characteristics revealed in this study can refine constraints used to develop atmospheric and climate models for Mars.

Here, we examine the hemispheric distribution of Mars' annual-mean albedo and the role of influence that the MY25 global dust storm plays. Figure S17 in Supporting Information S1 compares the meridional profile of annual-mean albedo between the season containing the MY25 global dust storm and normal years. Albedo modifications caused by the global dust storm (i.e., decreased albedo in the southern polar region and increased albedo elsewhere) are similar in both the seasonal and annual analyses (Figures S16 and S17 in Supporting Information S1). Since modifications to the albedo occur mainly in the autumn of MY25, its impact is diluted in the annual analysis, making the seasonal modification (Figure S16 in Supporting Information S1) more pronounced than the annual modification (Figure S17 in Supporting Information S1). Figure S17 in Supporting Information S1 can be also used to assess whether the MY25 global dust storm contributed to balancing the annual-mean albedo between the NH and SH. For MY25, the annual hemispheric-average albedos are 0.275 and 0.228, respectively. The NH albedo is larger than the SH albedo by ~ 0.047 ($\sim 20.6\%$ of the SH albedo) and is much larger than the albedo uncertainty ($\sim 5.0\%$). In normal years, hemispheric-average albedos are 0.267 and 0.215 for the NH and SH, respectively, or rather the albedo of the NH exceeds the SH by ~ 0.052 ($\sim 24.2\%$ of the SH albedo). Thus, the global dust storm in MY25 reduced hemispheric asymmetry in the annual-mean albedo from $\sim 24.2\%$ to $\sim 20.6\%$, which is substantially larger than the persistent $\sim 0.15\%$ asymmetry found on Earth and does not fully balance the albedo between the two hemispheres.

4. Conclusion and Discussion

We have presented the first meridional distribution of Mars' REB at seasonal and annual timescales. Additionally, a comparative analysis of the REBs of Mars and Earth at seasonal and annual scales was conducted. Their meridional distributions are dramatically different due to variations in surface, atmospheric, and orbital properties. Earth, a vibrant world with a thick atmosphere and an ocean of liquid water, facilitates meridional heat transport. In contrast, Mars lacks a liquid ocean and possesses a thin atmosphere. Earth's robust heat transport capacity results in meridional energy budget profiles with tropical energy excesses that diminish poleward into a deficit. Conversely, the dominant feature of Mars' seasonal REB is the presence of energy excesses in the higher latitudes of the spring and summer hemispheres with deficits in the polar night region at the opposite pole. Midlatitude and tropical regions exhibit a near neutral meridional distribution south of the equator and a slight deficit northward of the equator. Additionally, the eccentricity of the Martian orbit causes the polar REB maxima to vary in magnitude significantly due to insolation differences between perihelion and aphelion. At the annual scale, the meridional profiles of Mars' REB form a dip (a "U" shape) with the minimum around the equator. In contrast, Earth's corresponding profile would be similar but inverted and vertically stretched. Finally, our investigations suggest that global dust storms, a unique large-scale weather phenomenon on Mars, play a significant role in modifying the planet's REB.

As the meridional distribution of the REB is crucial for understanding a planet's atmosphere and climate. We anticipate that the new observational characteristics of the meridional distribution of Mars' REB at seasonal and annual timescales can enhance our understanding of the Martian system. Aiming to stimulate further ideas and studies, we briefly discuss a few potential applications of the Martian REB's meridional distribution.

One consideration for future studies concerning Mars' general circulation is the role of the REB in influencing large-scale meridional circulation and dust storm formation. Conventionally, the large-scale meridional

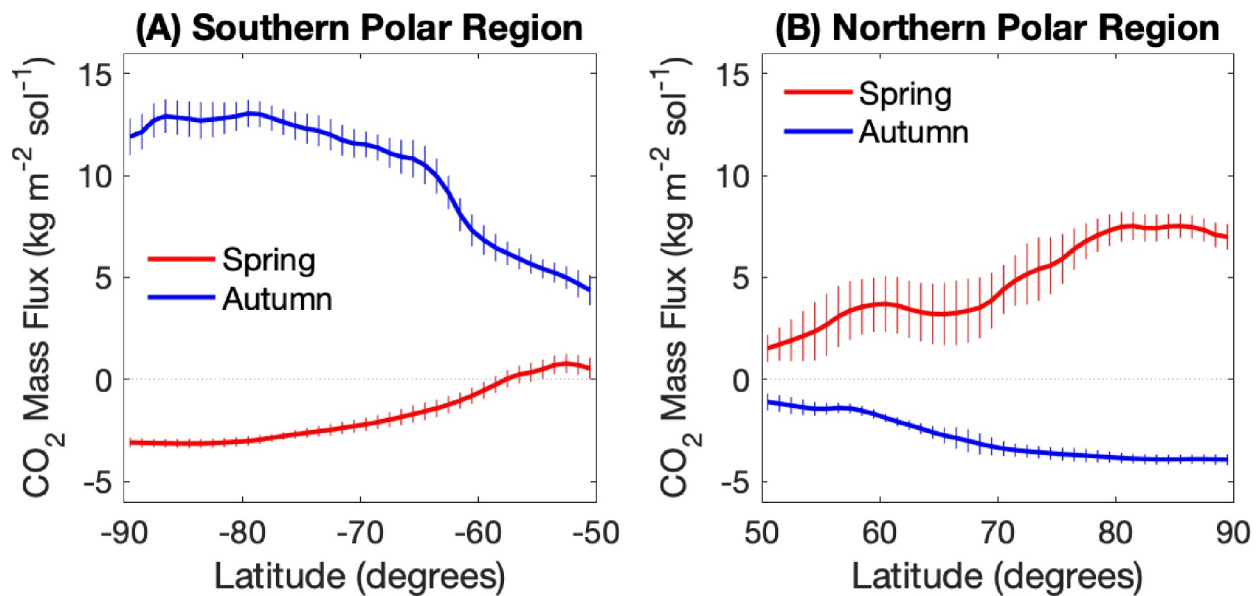


Figure 7. Meridional profiles of Martian daily carbon dioxide mass flux across the typical latitudes of each polar cap (50° – 90°) during the equinoctial seasons. The red curve corresponds to L_s 0° – 90° (NH spring and SH autumn) and the blue curves 180° – 270° (NH autumn and SH spring). (a) South polar region; (b) north polar region. A positive mass flux indicates the sublimation of CO_2 , while the negative mass flux represents the deposition of CO_2 . Vertical lines represent uncertainties in mass flux.

circulation of Mars has been attributed to the meridional distribution of insolation at the surface and its evolution over time (e.g., Ward, 1974; Zurek et al., 1992). Additionally, the Martian dichotomy has also been suggested as a mechanism capable of generating the observed seasonal variations in meridional circulation independent of the timing of perihelion (e.g., Richardson & Wilson, 2002). It is possible that the net effect of the REB, rather than insolation alone, combined with topographic forcing, can enhance our understanding and improve the fidelity of models for Mars' meridional circulation. In turn, the meridional distribution of the REB likely plays a critical role in creating the 'dusty' conditions of L_s 180° – 360° on Mars. In particular, panel C of Figure 3 shows that relatively large energy excess exists in the whole SH during its spring season ($L_s = 270^{\circ}$ – 360°). This significant energy excess can warm up the surface and hence the atmospheric layer near the surface, further creating convectively unstable conditions. Such instabilities probably play a role in developing dust storms over the whole SH.

Another potential application of our REB reanalysis is on the Martian CO_2 cycle, since the energy excess and deficit in the polar region can respectively contribute to the sublimation and deposition of CO_2 (e.g., Paige & Ingersoll, 1985; Schmidt et al., 2010; Titus et al., 2017). Here, a simple estimate of the CO_2 mass flux can be made by assuming that all of the excess and deficit in the REB (Figure 3) are utilized to sublimate and deposit CO_2 respectively. With such an assumption, we can convert the REB profiles shown in Figure 3 into profiles of CO_2 mass fluxes through dividing each profile by the latent heat of CO_2 sublimation/deposition (571,300 J/kg). Spatially, only high latitudes are considered, because relatively little solid CO_2 exists equatorward of 50° . Temporally, only the equinoctial seasons (spring and autumn) are examined, as CO_2 phase changes are most dominant during these periods. During these seasons, the growth and recession of the seasonal polar caps are most rapid, and the flux of mass into and out of the polar regions highest. In contrast, the sizes of the seasonal caps remain relatively stable throughout most of summer and winter, despite these being the warmest and coldest periods, respectively.

As anticipated from applying a scalar uniformly to Figure 3, the southern cap liberates more CO_2 than the northern cap overall (Figure 7). Deposition rates, on the other hand, are comparable between the two polar caps. Quantitatively, the mass fluxes have rough agreement with prior studies within one order of magnitude (Kieffer et al., 2000; Kieffer & Titus, 2001; Titus et al., 2017). While our simple estimate suggests that the REB is an important factor in the CO_2 cycle in the high latitudes, there are other factors that must be accounted for. For example, part of the energy excess and deficit in the REB can modify the surface temperature, which could be ice, before the sublimation and deposition of CO_2 occurs. Another consideration is the interactive relationship

between the REB and the CO₂ phase change: while the REB directly affects CO₂ sublimation/deposition rates, corresponding growth and recession of the ice caps cause changes in the visible and thermal characteristics of the surface, hence modifying the REB. Summarily, the REB provides an important constraint for the Martian CO₂ cycle, especially at the poles, which should be considered in future studies of Mars' surface, atmosphere, and climate.

Conflict of Interest

The authors declare no conflicts of interest relevant to this study.

Data Availability Statement

MGS-TES data outputs are available publicly online from its data archive (http://tes.asu.edu/data_tool/). The CERES-EBAF data used in this study are publicly available online from the NASA Langley Research Center and can be downloaded (Doelling, 2022). Basic numerical parameters relating to Mars and Earth are cited from the NASA Planetary Fact Sheet (<https://nssdc.gsfc.nasa.gov/planetary/factsheet/index.html>).

Acknowledgments

We express our gratitude to the teams of MGS-TES and CERES-EBAF for recording, processing, and archiving extensive data sets, which enables the comparative study concerning the Radiant Energy Budget (REB) between Mars and Earth.

References

- Atreya, S. K., Pollack, J. B., & Matthews, M. S. (Eds.) (1989). *Origin and evolution of planetary and satellite atmospheres*. University of Arizona Press.
- Battalio, M., & Wang, H. (2021). The Mars dust activity database (MDAD): A comprehensive statistical study of dust storm sequences. *Icarus*, 354, 114059. <https://doi.org/10.1016/j.icarus.2020.114059>
- Bell, J. F., Rice, M. S., Johnson, J. R., & Hare, T. M. (2008). Surface albedo observations at Gusev crater and Meridiani Planum, Mars. *Journal of Geophysical Research*, 113(E6), e06s18. <https://doi.org/10.1029/2007je002976>
- Boeira Dias, F., Fiedler, R., Marsland, S. J., Domingues, C. M., Clément, L., Rintoul, S. R., et al. (2020). Ocean heat storage in response to changing ocean circulation processes. *Journal of Climate*, 33(21), 9065–9082. <https://doi.org/10.1175/jcli-d-19-1016.1>
- Byrne, S. (2009). The polar deposits of Mars. *Annual Review of Earth and Planetary Sciences*, 37(1), 535–560. <https://doi.org/10.1146/annurev.earth.031208.100101>
- Byrne, S., Zuber, M. T., & Neumann, G. A. (2008). Interannual and seasonal behavior of Martian residual ice-cap albedo. *Planetary and Space Science*, 56(2), 194–211. <https://doi.org/10.1016/j.pss.2006.03.018>
- Cantor, B. A., James, P. B., Caplinger, M., & Wolff, M. J. (2001). Martian dust storms: 1999 Mars orbiter camera observations. *Journal of Geophysical Research*, 106(E10), 23653–23687. <https://doi.org/10.1029/2000je001310>
- Christensen, P. R., Anderson, D. L., Chase, S. C., Clancy, R. T., Clark, R. N., Conrath, B. J., et al. (1998). Results from the Mars global surveyor thermal emission spectrometer. *Science*, 279(5357), 1692–1698. <https://doi.org/10.1126/science.279.5357.1692>
- Christensen, P. R., Bandfield, J. L., Hamilton, V. E., Ruff, S. W., Kieffer, H. H., Titus, T. N., et al. (2001). Mars global surveyor thermal emission spectrometer experiment: Investigation description and surface science results. *Journal of Geophysical Research*, 106(E10), 23823–23871. <https://doi.org/10.1029/2000je001370>
- Creecy, E. C., Li, L., Jiang, X., Smith, M., Kass, D., Kleinböhl, A., & Martínez, G. (2022). Mars' emitted energy and seasonal energy imbalance. *Proceedings of the National Academy of Sciences of the United States of America*, 119(21), e2121084119. <https://doi.org/10.1073/pnas.2121084119>
- Datsis, G., & Stevens, B. (2021). Earth's albedo and its symmetry. *AGU Advances*, 2(3), e2021AV000440. <https://doi.org/10.1029/2021av000440>
- Doelling, D. (2022). CERES Energy Balanced and Filled (EBAF) TOA Monthly means data in netCDF Edition4.2 [Dataset]. *NASA Langley Atmospheric Science Data Center Distributed Active Archive Center*. https://doi.org/10.5067/TERRA-AQUA-NOAA20/CERES/EBAF-TOA_L3B004.2
- Ellis, J. S., & Vonder Haar, T. H. (1976). *Zonal average Earth radiation budget measurements from satellites for climate studies*. (NASA Contractor Tech. Rep. 240). Colorado State University.
- Gurwell, M. A., Bergin, E. A., Melnick, G. J., & Tolls, V. (2005). Mars surface and atmospheric temperature during the 2001 global dust storm. *Icarus*, 175(1), 23–31. <https://doi.org/10.1016/j.icarus.2004.10.009>
- Guzewich, S. D., Lemmon, M., Smith, C. L., Martínez, G., de Vicente-Retortillo, Á., Newman, C. E., et al. (2019). Mars Science Laboratory observations of the 2018/Mars year 34 global dust storm. *Geophysical Research Letters*, 46(1), 71–79. <https://doi.org/10.1029/2018gl080839>
- Haberle, R. M., & Kahre, M. A. (2010). Detecting secular climate change on Mars. *Mars*, 5, 68–75. <https://doi.org/10.1555/mars.2010.0003>
- Hansen, J., Nazarenko, L., Ruedy, R., Sato, M., Willis, J., del Genio, A., et al. (2005). Earth's energy imbalance: Confirmation and implications. *Science*, 308(5727), 1431–1435. <https://doi.org/10.1126/science.1110252>
- Holmes, J. A., Lewis, S. R., & Patel, M. R. (2019). OpenMARS database [Dataset]. *The Open University Collection*. <https://doi.org/10.21954/ou.rd.c.4278950>
- Holmes, J. A., Lewis, S. R., & Patel, M. R. (2020). OpenMARS: A global record of Martian weather from 1999 to 2015. *Planetary and Space Science*, 188, 104962. <https://doi.org/10.1016/j.pss.2020.104962>
- Hourdin, F., Le Van, P., Forget, F., & Talagrand, O. (1993). Meteorological variability and the annual surface pressure cycle on Mars. *Journal of the Atmospheric Sciences*, 50(21), 3625–3640. [https://doi.org/10.1175/1520-0469\(1993\)050<3625:mvasat>2.0.co;2](https://doi.org/10.1175/1520-0469(1993)050<3625:mvasat>2.0.co;2)
- Kelly, N. J., Boynton, W. V., Kerry, K., Hamara, D., Janes, D., Reedy, R. C., et al. (2006). Seasonal polar carbon dioxide frost on Mars: CO₂ mass and columnar thickness distribution. *Journal of Geophysical Research*, 111(E3), E03S07. <https://doi.org/10.1029/2006je002678>
- Kieffer, H. H., & Titus, T. (2001). TES mapping of Mars' north seasonal cap. *Icarus*, 154(1), 162–180. <https://doi.org/10.1006/icar.2001.6670>
- Kieffer, H. H., Titus, T. N., Mullins, K. F., & Christensen, P. R. (2000). Mars south polar spring and summer behavior observed by TES: Seasonal cap evolution controlled by frost grain size. *Journal of Geophysical Research*, 105(E4), 9653–9699. <https://doi.org/10.1029/1999je001136>

- L'Ecuyer, T. S., Beaudoin, H. K., Rodell, M., Olson, W., Lin, B., Kato, S., et al. (2015). The observed state of the energy budget in the early twenty-first century. *Journal of Climate*, 28(21), 8319–8346. <https://doi.org/10.1175/jcli-d-14-00556.1>
- Li, L., Baines, K. H., Smith, M. A., West, R. A., Pérez-Hoyos, S., Trammell, H. J., et al. (2012). Emitted power of Jupiter based on Cassini CIRS and VIMS observations. *Journal of Geophysical Research*, 117(E11), E11002. <https://doi.org/10.1029/2012je004191>
- Li, L., Conrath, B. J., Gierasch, P. J., Achterberg, R. K., Nixon, C. A., Simon-Miller, A. A., et al. (2010). Saturn's emitted power. *Journal of Geophysical Research*, 115(E11), E11002. <https://doi.org/10.1029/2010je003631>
- Li, L., Nixon, C. A., Achterberg, R. K., Smith, M. A., Gorius, N. J. P., Jiang, X., et al. (2011). The global energy balance of Titan. *Geophysical Research Letters*, 38(23), L23201. <https://doi.org/10.1029/2011gl050053>
- Loeb, N. G., Doelling, D. R., Wang, H., Su, W., Nguyen, C., Corbett, J. G., et al. (2018). Clouds and the Earth's radiant energy system (CERES) energy balanced and filled (EBAF) top-of-atmosphere (TOA) edition 4.0 data product. *Journal of Climate*, 31(2), 895–918. <https://doi.org/10.1175/jcli-d-17-0208.1>
- Martínez, G. M., Newman, C. N., De Vicente-Retortillo, A., Fischer, E., Renno, N. O., Richardson, M. I., et al. (2017). The modern near-surface Martian climate: A review of in-situ meteorological data from viking to curiosity. *Space Science Reviews*, 212(1–2), 295–338. <https://doi.org/10.1007/s11214-017-0360-x>
- Martínez, G. M., Sebastián, E., Vicente-Retortillo, A., Smith, M. D., Johnson, J. R., Fischer, E., et al. (2023). Surface energy budget, albedo, and thermal inertia at Jezero Crater, Mars, as observed from the Mars 2020 MEDA instrument. *Journal of Geophysical Research: Planets*, 128(2), e2022JE007537. <https://doi.org/10.1029/2022je007537>
- Paige, D. A., & Ingersoll, A. P. (1985). Annual heat balance of Martian polar caps: Viking observations. *Science*, 228(4704), 1160–1168. <https://doi.org/10.1126/science.228.4704.1160>
- Peixoto, J. P., & Oort, A. H. (1992). *Physics of climate*. American Institute of Physics.
- Piqueux, S., Kleinböhl, A., Hayne, P. O., Kass, D. M., Schofield, J. T., & McCleese, D. J. (2015). Variability of the Martian seasonal CO₂ cap extent over eight Mars Years. *Icarus*, 251, 164–180. <https://doi.org/10.1016/j.icarus.2014.10.045>
- Read, P. L., Barstow, J., Charnay, B., Chelvanithilan, S., Irwin, P. G. J., Knight, S., et al. (2016). Global energy budgets and 'Trenberth diagrams' for the climates of terrestrial and gas giant planets. *Quarterly Journal of the Royal Meteorological Society*, 142(695), 703–720. <https://doi.org/10.1002/qj.2704>
- Richardson, M. I., & Wilson, R. J. (2002). A topographically forced asymmetry in the Martian circulation and climate. *Nature*, 416(6878), 298–301. <https://doi.org/10.1038/416298a>
- Sánchez-Lavega, A., del Río-Gaztelurrutia, T., Hernández-Bernal, J., & Delcroix, M. (2019). The onset and growth of the 2018 Martian global dust storm. *Geophysical Research Letters*, 46(11), 6101–6108. <https://doi.org/10.1029/2019gl083207>
- Schmidt, F., Schmitt, B., Douté, S., Forget, F., Jian, J.-J., Martin, P., et al. (2010). Sublimation of the Martian CO₂ seasonal south polar cap. *Planetary and Space Science*, 58(10), 1129–1138. <https://doi.org/10.1016/j.pss.2010.03.018>
- Schneider, T., Bischoff, T., & Haug, G. H. (2014). Migrations and dynamics of the intertropical convergence zone. *Nature*, 513(7516), 45–53. <https://doi.org/10.1038/nature13636>
- Schubert, G., & Mitchell, J. L. (2014). *Comparative climatology of terrestrial planets* (pp. 181–191). University of Arizona Press.
- Smith, M. D. (2004). Interannual variability in TES atmospheric observations of Mars during 1999–2003. *Icarus*, 167(1), 148–165. <https://doi.org/10.1016/j.icarus.2003.09.010>
- Smith, M. D., Conrath, B. J., Pearl, J. C., & Christensen, P. R. (2001). Thermal Emission Spectrometer observations of Martian planet-encircling dust storm 2001A. *Icarus*, 157, 259–263.
- Stephens, G. L., O'Brien, D., Webster, P. J., Pilewski, P., Kato, S., & Li, J. L. (2015). The albedo of Earth. *Reviews of Geophysics*, 53(1), 141–163. <https://doi.org/10.1002/2014rg000449>
- Stocker, T. F., Qin, D., Plattner, G.-K., Tignor, M., Allen, S. K., Boschung, J., et al. (Eds.) (2013). *Climate change 2013: The physical science basis. Contribution of working group I to the fifth assessment report of the intergovernmental panel on climate change*. Cambridge University Press.
- Strausberg, M. J., Wang, H., Richardson, M. I., Ewald, S. P., & Toigo, A. D. (2005). Observations of the initiation and evolution of the 2001 Mars global dust storm. *Journal of Geophysical Research*, 110(E2), E02006. <https://doi.org/10.1029/2004je002361>
- Titus, T. N., Byrne, S., Colaprete, A., Forget, F., Michaels, T. I., & Prettyman, T. H. (2017). The CO₂ cycle. In R. M. Haberle, R. T. Clancy, F. Forget, M. D. Smith, & R. W. Zurek (Eds.), *The atmosphere and climate of Mars* (pp. 374–404). Cambridge University Press.
- Trenberth, K. E., Fasullo, J. T., Von Schuckmann, K., & Cheng, L. (2016). Insights into Earth's energy imbalance from multiple sources. *Journal of Climate*, 29(20), 7495–7505. <https://doi.org/10.1175/jcli-d-16-0339.1>
- Vonder Haar, T. H., Stephens, G. L., & Campbell, G. G. (1980). *Earth radiation budget measurements from satellites and their interpretation for climate modeling and studies*. (NASA Contractor Tech. Rep. 159232). Goddard Space Flight Center.
- Ward, W. R. (1974). Climatic variations on Mars: 1. Astronomical theory of insolation. *Journal of Geophysical Research*, 79(24), 3375–3486. <https://doi.org/10.1029/jc079i024p03375>
- Zurek, R. W., Barnes, J. R., Haberle, R. M., Pollack, J. B., Tillman, J. E., & Leovy, C. B. (1992). Dynamics of the atmosphere of Mars. In H. H. Kieffer, B. M. Jakosky, C. W. Snyder, & M. S. Matthews (Eds.), *Mars* (pp. 835–933). University of Arizona Press.
- Zurek, R. W., & Martin, L. J. (1993). Interannual variability of planet-encircling dust storms on Mars. *Journal of Geophysical Research*, 98(E2), 3247–3259. <https://doi.org/10.1029/92je02936>